Helicon wave coupling in KSTAR plasmas for off-axis current drive in high electron pressure plasmas

View the article online for updates and enhancements.

Helicon wave coupling in KSTAR plasmas for off-axis current drive in high electron pressure plasmas

S.J. Wang, H.H. Wi, H.J. Kim, J. Kim, J.H. Jeong and J.G. Kwak

NFRI, Daejeon, 34133, Korea

E-mail: sjwang@nfri.re.kr

CrossMark

Abstract

A helicon wave current drive is proposed as an efficient off-axis current drive in the high electron β plasmas that are expected in fusion reactors. A high frequency helicon wave coupling was analyzed using the surface impedance at a plasma boundary. A slow wave coupling, which may compete with the helicon wave coupling at a frequency of 500 MHz, is estimated to be lower than the fast wave coupling by an order of magnitude in the KSTAR edge plasma density and in practical Faraday shield misalignment with the magnetic pitch. A traveling wave antenna, which is a two port combline antenna, was analyzed using a simplified lumped element model. The results show that the traveling wave antenna provides load resiliency because of its insensitivity to loading resistance, provided that the loading resistance at a radiating element is limited within a practical range. The combline antenna is attractive because it does not require a matching system and exhibits a high selectivity of parallel refractive index. Based on the analysis, a seven element combline antenna was fabricated and installed at an off-mid-plane offset of 30 cm from the mid-plane in KSTAR. The low power RF characteristics measured during several plasma discharges showed no evidence of slow wave coupling. This is consistent with the expectation made through the surface impedance analysis which predicted low slow wave coupling. The wave coupling to the plasma is easily controlled by a radial outer-gap control and gas puffing. No plasma confinement degradation was observed during the radial outer-gap control of up to 3 cm in H-mode discharges. In a ELMy plasmas, only a small reflection peak was observed during a very short portion of the ELM bursting period. If the number of radiating elements is increased for high power operation, then complete load resiliency can be expected. A very large coupling can be problematic for maintaining a parallel refractive index, although this issue can be mitigated by increasing the number of elements.

Keywords: KSTAR, helicon, current drive, high frequency fast wave, TWA, combline antenna

(Some figures may appear in colour only in the online journal)

1. Introduction

The use of auxiliary methods in non-inductive current drives is considered to be essential to achieve steady state plasma operation in tokamaks to complement the bootstrap current [1]. A non-inductive current drive can be realized using various heating and current drive systems, such as neutral beam injection (NBI), fast wave current drive (FWCD), lower hybrid current drive (LHCD), and electron cyclotron current drive (ECCD) [2–6]. Among these systems, the LHCD appears to have a high current drive efficiency with a far off-axis current drive capability [7, 8]. However, the problem of LHCD efficiency in high density plasmas [7, 9] is still open to investigation. The driven current peaks in the plasma periphery [4, 6] in a high density and temperature plasma. A helicon wave current drive (HCD) has been proposed as a solution to

overcome the limitations of the LHCD because HCD exhibits an efficient mid-radius current drive capability for the high β plasmas that are expected in fusion reactors [1, 10–13].

A high frequency helicon wave, which can be described by the frequency range $\omega_{ci} \ll \omega \lesssim \omega_{LH}$, where ω, ω_{ci}, and ω_{LH} are the wave frequency, ion cyclotron frequency, and lower hybrid frequency, respectively, is essentially a fast wave among two wave modes in a cold plasma. A fast wave launched from the plasma periphery has a longer path to the plasma center when compared to that of a lower frequency fast wave as a result of the strong tendency to align with a static magnetic field. The helical wave motion becomes strong in high density plasmas. Another characteristic of the helicon wave is that it has a moderate optical thickness so as to obtain maximum damping at the mid-radius of the plasma in medium- and large-size tokamaks when an adequate electron β is present. Several predictions have shown that an HCD is quite promising for KSTAR, DIII-D, ITER, FNST, and some DEMO grade plasmas [11–13].

It is well known that there is an issue with the fast wave coupling from an antenna to a bulk plasma through a scrape-off layer (SOL) plasma due to the presence of a wave evanescent layer in the plasma periphery [14]. In a high frequency range, the thickness of the launched fast wave evanescent layer is greater than that of lower frequency fast wave at the fundamental or several harmonics of ω_{ci} because the cutoff density n_{cF} is linearly dependent on ω. Therefore, identification of the wave coupling capability at the high frequency is essential for the development of high power HCD systems.

In this high frequency HCD regime, a slow wave can propagate at a plasma density ($n_e \sim 1 \times 10^{15}\,\text{m}^{-3}$) that is two or three orders of magnitude lower than typical far SOL density in KSTAR. Therefore, it is reasonable to consider the power competition between the fast and slow waves.

A traveling wave antenna (TWA) is an attractive option because of its insensitivity to loading resistance R_L [15–18]. The reduction of R_L for each element and the increase in the number of elements reduces the R_L sensitivity of the TWA. In addition, increasing the number of elements increases the selectivity of the parallel refractive index $n_\parallel$. The only factor that limits the number of elements in the TWA is the toroidal dimension of the antenna. The TWA can be matched to the characteristic impedance of the transmission line without additional tuning elements because there is a matched load at the output port. The matched antenna system reduces the peak voltage and current in the transmission line, and thereby simplifies the power transmission system.

In section 2, the plasma surface impedance is analyzed to predict the slow and fast wave couplings. The relative amount of slow wave coupling is estimated to be small in realistic plasma conditions. The plasma surface impedance couples the fast wave polarization to the slow wave polarization and vice versa. Therefore, the wave coupling effect can also be analyzed. In section 3, a simplified circuit analysis for the TWA is presented that focuses on the insensitivity to the loading resistance. The experimental setup and basic performance of a fabricated mock-up TWA is described in section 4. In section 5, a coupling measurement performed in KSTAR discharges is

discussed. The main focus points are the controllability of the coupling in terms of the radial outer-gap and local gas puffing, the load resiliency of the TWA, and the effect of a Faraday shield angle with respect to the magnetic pitch, which may identify slow wave coupling. The summary and conclusion follow in section 6.

2. Fast wave coupling

In a frequency range that is much lower than the electron plasma frequency ω_{pe} and the electron cyclotron frequency ω_{ce}, the dispersion relation of waves can be written as a function of the parallel refractive index $n_\parallel$ following Stix notation as [19]

$$n_{\perp F}^2 = -\frac{(n_\parallel^2 - R)(n_\parallel^2 - L)}{n_\parallel^2 - S}, \tag{1}$$

$$n_{\perp S}^2 = -(n_\parallel^2 - S)\frac{P}{S}, \tag{2}$$

where $n_{\perp F}$ and $n_{\perp S}$ are the perpendicular refractive indices for the fast and slow wave branches in a cold plasma, respectively. The coefficients are

$$S = \frac{1}{2}(R + L), \tag{3}$$

$$R = 1 - \sum_s \frac{\omega_{ps}^2}{\omega(\omega + \omega_{cs})}, \tag{4}$$

$$L = 1 - \sum_s \frac{\omega_{ps}^2}{\omega(\omega - \omega_{cs})}, \tag{5}$$

$$P = 1 - \sum_s \frac{\omega_{ps}^2}{\omega^2}, \tag{6}$$

where ω_{cs} and ω_{ps} are the cyclotron frequency and plasma frequency, respectively, of the particle species s.

The R cutoff density n_{cF} of the fast wave defined by $n_\parallel^2 - R = 0$ in equation (1) can be expressed as

$$n_{cF} \sim \frac{\epsilon_0}{e} B_0 \omega n_\parallel^2, \tag{7}$$

where B_0 is the static magnetic field. Equation (7) indicates that the thickness of the evanescent layer in front of a fast wave launcher is linearly dependent on ω if the optimum $n_\parallel$ [10, 20] for efficient electron heating and current drive in the same plasma conditions is chosen, such as the parallel phase velocity $c/n_\parallel$, which is similar to the electron thermal velocity.

In an evanescent layer, a launched fast wave may decay along the x direction as $\exp(-k_0\nu_\perp x)$, where $k_0 = \omega/c$ and $\nu_\perp = in_\perp$ when $n_\perp^2 < 0$. Figure 1 shows the fast wave decay length defined by the $e - \text{folding}$ length $l_d = 1/k_0\nu_\perp$ with $n_\parallel = 3$. The decay length l_d decreases slowly at a certain density, and rapidly decreases at lower frequencies. The sharp increase at the lower bound of the frequency means that the
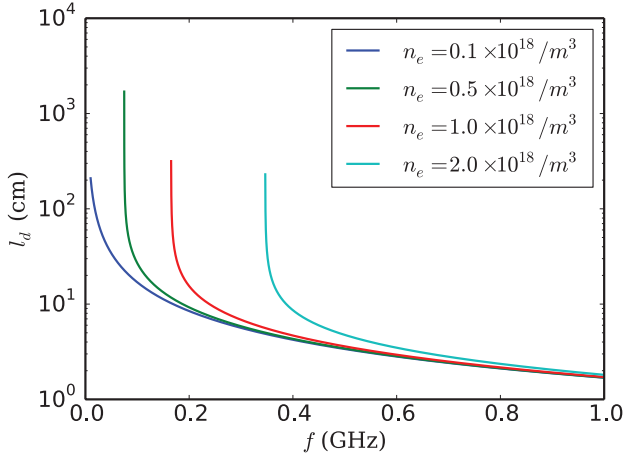
Figure 1. The $e-$folding decay length of a fast wave for various plasma densities.
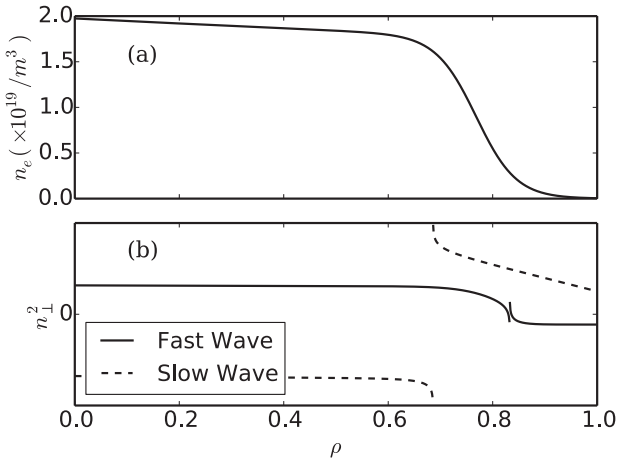
Figure 2. (*a*) Plasma density profile, which corresponds to (*b*) $n_\perp^2$ of the fast and slow waves at 500 MHz.

wave propagates at a frequency lower than this frequency bound. Furthermore, l_d depends weakly on the density at higher frequencies.

As ω increases to ω_{LH}, the slow wave is able to propagate from the antenna to the plasma bulk. When the slow wave dispersion relation shown in equation (2) is combined with equation (6), it is evident that the slow wave is able to propagate if $\omega < \omega_{pe}$. If $\omega/2\pi = 500$ MHz, the slow wave cutoff corresponds to $n_e < 3.1 \times 10^{15}\,\mathrm{m}^{-3}$. Figure 2 shows $n_\perp^2$ for both waves and the corresponding plasma density profiles for $B_0 = 2$ T at $\omega/2\pi = 500$ MHz. The slow wave propagates at the outer edge of the plasma to the lower hybrid resonance at the normalized radius $\rho \sim 0.7$, in contrast to the fast wave which has a thick evanescent layer in the periphery. Therefore, it may be reasonable to consider that the slow wave can be coupled from the launcher to the plasma bulk. This feature causes concerns regarding a power competition between the slow and fast waves, or a possible deterioration of the power coupling to the plasma due to the resonant behavior of the slow wave at a lower hybrid resonance.
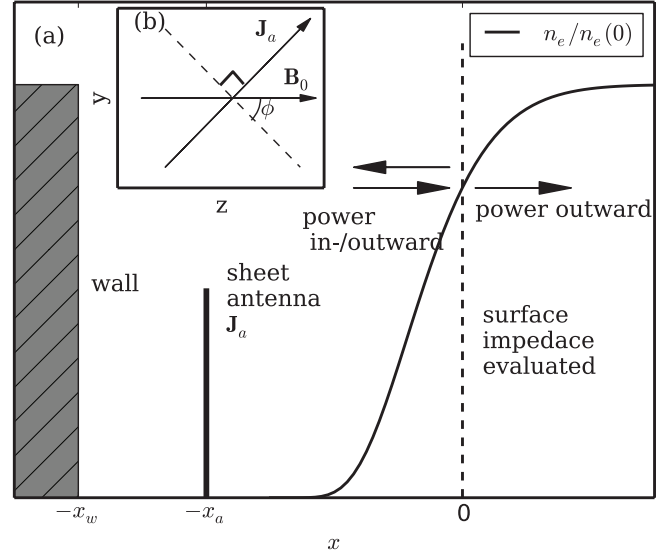
Figure 3. Schematic illustrating the wave coupling model.

The RF surface impedance of the plasma [21–23] provides useful information for the analysis of the wave coupling from the antenna to the plasma core through the low density plasma periphery. The surface impedance, which is defined by the linear relation between the tangential components of the electric field and the magnetic field, completely characterizes the plasma in terms of the wave propagation, provided that wave causality is considered.

In the restricted case that involves no other wave sources except for the antenna, and no inward radiation from the plasma, i.e. the waves either propagate to infinity or are fully absorbed, the surface impedance can be solved analytically.

Figure 3 shows a schematic of the boundary conditions used for a coupling analysis through the surface impedance following Brambilla [23]. A wave launched at the antenna undergoes an evanescent decay up to the cutoff density and then propagates in the plasma. At the plasma surface at $x = 0$ where the surface impedance must be evaluated, a portion of the power is reflected while the remaining power is transmitted into the plasma. No reflection occurs from the interior of the plasma. The region $x < 0$ is regarded as a vacuum, $n_x^2 + n_y^2 + n_z^2 = 1$, where n_x, n_y and n_z are the vector components of the refractive index in the Cartesian coordinate system. The loading resistance in each wave mode can be written using the power flux $P_{x\alpha}$ derived in the appendix as

$$R_{L\alpha} = \frac{2P_{x\alpha}}{|I_a|^2},\qquad(8)$$

where α denotes the fast(F) or slow(S) mode, and I_a is the antenna current.

Figure 4, which displays $n_{\perp\alpha}^2$ with $n_z = 3$ as a function of n_e, shows that the slow wave cutoff density is $\sim 3.1 \times 10^{15}\,\mathrm{m}^{-3}$ and the fast wave cutoff density is $\sim 3 \times 10^{18}\,\mathrm{m}^{-3}$. These results coincide with the slow wave cutoff condition $\omega = \omega_{pe}$ and equation (7). It can be estimated that there is a negligible slow wave evanescent layer between the antenna and plasma, in contrast to the fast wave, which forms an evanescent
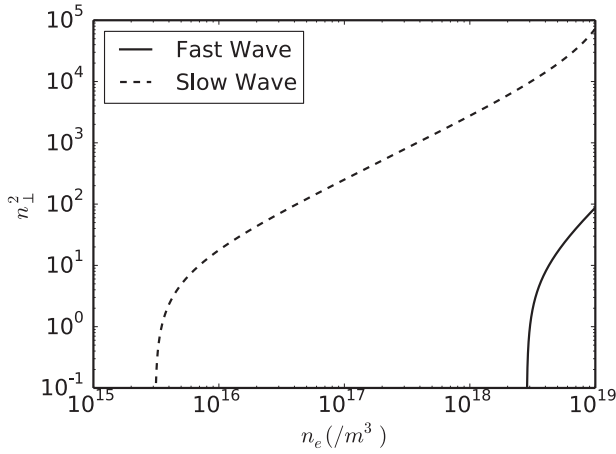
Figure 4. The $n_\perp^2$ of fast and slow waves for $n_\parallel = 3$. The slow wave propagates above $n_e = 3.1 \times 10^{15}$ m^{-3} and the fast wave propagates above $n_e = 3 \times 10^{18}$ m^{-3}.

layer that is a few centimeters thick. Figure 5 shows $R_{L\alpha}$ for $B_T = 2$ T, $\omega/2\pi = 500$ MHz, $n_z = 3$, $n_y = 0$, $x_w = -7$ cm , and $x_a = -2$ cm. Figures 5(a)–(d) show the wave-decoupled cases for $\phi = 0°$, 10°, 45°, and 90°, respectively, and (e)–(h) show the coupled cases for the same series of ϕ, where ϕ is the angle difference between the normal antenna current and static magnetic field. It is clear that at $\phi = 0°$ or 90°, only the fast or the slow wave is coupled, regardless of the coupled or decoupled modes. Although the fast wave evanescent layer is much thicker than that of the slow wave, in the meaningful range of n_e for SOL plasma, the fast wave coupling is much higher than slow wave coupling regardless of the mode coupling, provided that $\phi < 45°$. However, the coupling difference between the modes is smaller when the modes are coupled. Figure 5(f) shows that a cross-over between the modes occurs near $n_e \sim 1 \times 10^{17}$ m^{-3}, which is much lower than the expected density in SOL plasma [24] with a 10° misalignment of an antenna polarization for the fast wave.

Figure 6 shows a summary of the misalignment effect for the typical density, $n_e = 3 \times 10^{18}$ m^{-3}, and the plasma boundary, $x_a = -2$ cm, when the modes are coupled with $n_z = 3$. Below $\phi < 20°$, the ratio of the coupled slow wave power to the total power is less than 5%.

3. TWA

A TWA is a two-port antenna system with both input and output ports, in contrast to a conventional ICRF antenna that has only an input port. In the TWA, part of the power that is fed into the input port is radiated to space and the remaining power is transmitted to a dummy load connected to the output port. Therefore, the impedance of the antenna system can be maintained equal to the characteristic impedance of the system if the radiation is small compared to the transmission along the TWA. This feature enables the implementation of tuner-free or load-resilient antenna systems. According to the Floquet theory, the longitudinal wavelength of the TWA

can be controlled with small frequency variations because it usually has a periodic structure that generates a guided slow wave with $v_{ph} < c$, where v_{ph} is the phase speed of the guided wave and c is the speed of light. If the frequency bandwidth of the RF generator is adequate, a useful method to control the heating can be realized.

Among the various TWA types, a combline antenna was chosen for testing in KSTAR because it has already shown good performance in the JFT-2M tokamak [16, 25]. In the combline antenna shown in figure 7, the power fed to the input port generates an RF current at the first resonant current strap. The combination of the length of the strap and the capacitance at its open end was selected to ensure resonance at the center frequency. As is the general configuration for a TWA, a portion of the power is radiated and the remainder is mutually coupled to the neighboring strap. This radiation and coupling continues to the last strap connected to the dummy load, which has a resistance R_0 equal to the characteristic impedance Z_0 of the system. By simplifying the TWA with the lumped element circuit of figure 8 that has loading resistance R_L, conductor resistance R_c, self inductance L, capacitance C and mutual inductance M, the circuit can be analyzed with a simple approach. In this model, all current straps, except for the first and the last are assumed to be identical and only neighboring straps exhibit inductive mutual coupling. Then, the currents I_i flowing on each of the n straps can be written as,

$$-SI_1 + i\omega MI_2 = V_{in} \qquad (9)$$

$$i\omega MI_{i-1} - SI_i + i\omega MI_{i+1} = 0, \ i = 2, ...(n-1) \qquad (10)$$

$$i\omega MI_{n-1} - (S + R_0)I_n = 0, \qquad (11)$$

where the self current term S is, together with $R_t = R_L + R_c$, can be defined as

$$S = R_t + i\omega L - i\frac{1}{\omega C}. \qquad (12)$$

Because each strap is resonant at the center frequency ω_0, L, and C can be determined from the relation $L = 1/\omega_0^2 C$. Therefore, S in equation (12) can be further simplified as $S = R_t$ at ω_0.

It is trivial to solve equations (9)–(11) for I_i in matrix form. By using the resulting I_i, the impedance and power of each strap can be calculated. Figure 9 shows $Z_{in} = V_{in}/I_1$ versus R_t for various numbers of straps n at the center frequency ω_0. The element values $C = 1.12$ pF and $\omega_0 M = 4.7$ Ω were chosen from the comparison between the bandwidth calculated with this model and the fabricated TWA at $\omega_0/2\pi = 0.5$ GHz. The analytically calculated Z_{in} for the $n = 3$ case,

$$Z_{in} = R_t + R_0 \frac{\omega^2 M^2}{\omega^2 M^2 + R_t R_0}, \qquad (13)$$

is also shown for comparison purpose. For very small R_t, Z_{in} decreases rapidly; however, above a certain value that depends on n, Z_{in} is relatively constant. This property provides the load resiliency of the TWA. As n increases, the decrease of Z_{in} becomes sharper and the range of load resiliency widens. It
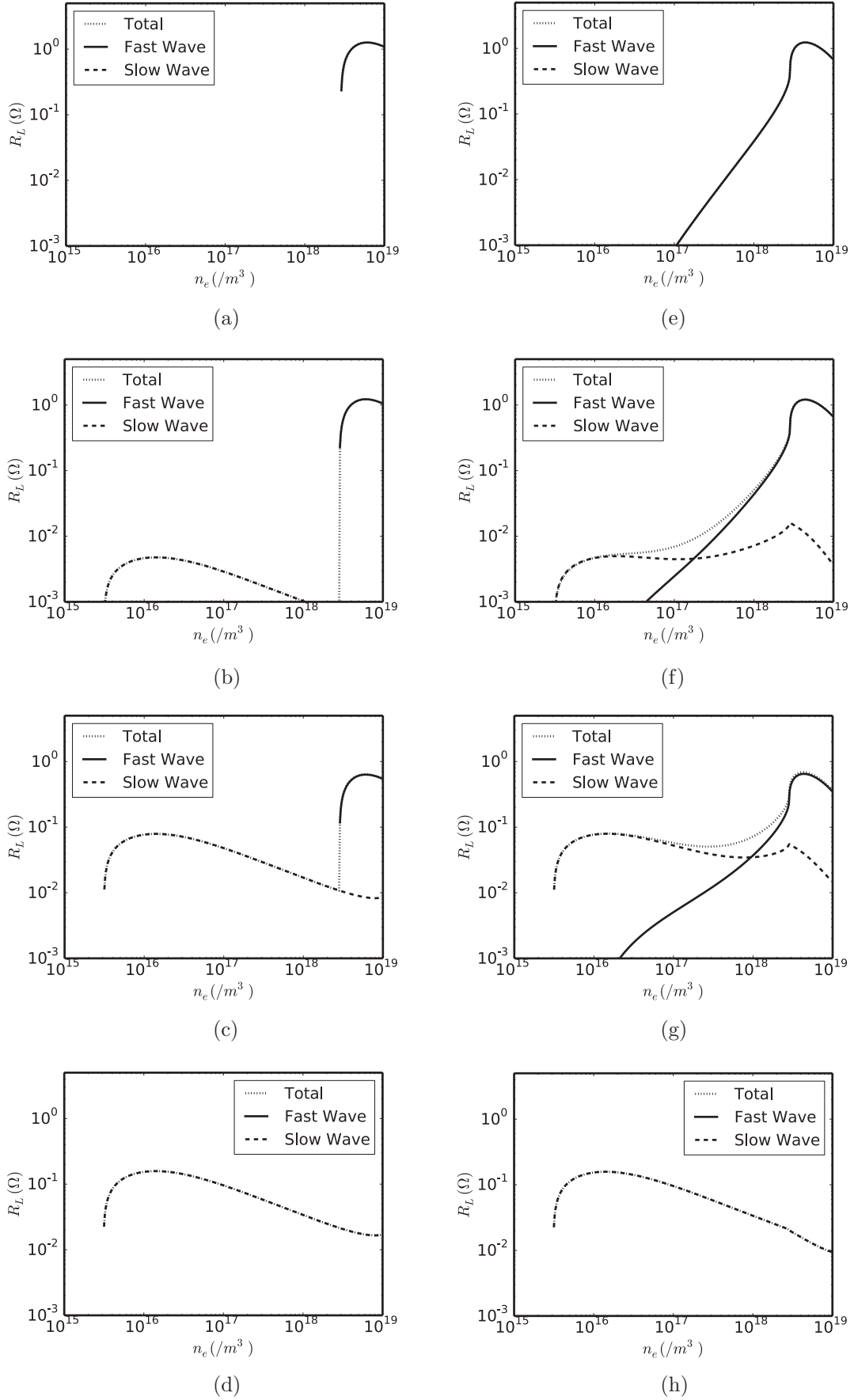
Figure 5. R_L of fast and slow decoupled waves for pitch angle misalignments of (*a*) 0°, (*b*) 10°, (*c*) 45°, and (*d*) 90° and the corresponding coupled cases for misalignments of (*e*) 0°, (*f*) 10°, (*g*) 45°, and (*h*) 90°. The parallel refractive index is $n_{\parallel} = 3$.
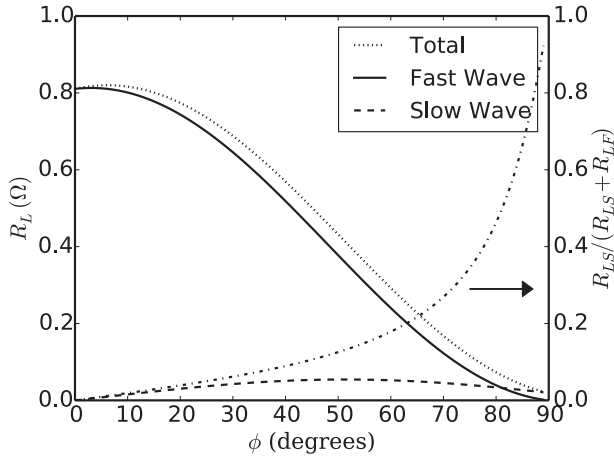
Figure 6. The R_L versus ϕ for coupled fast and slow waves. The right axis shows the slow wave portion.

is known that in the semi-infinite series ($n \to \infty$) of the TWA with $R_t \ll \omega M$, Z_{in} can be approximated by [26]

$$Z_{in} = \omega M \left[1 - \frac{1}{8} \left(\frac{R_t}{\omega M} \right)^2 + ... \right], \qquad (14)$$

which is nearly independent of R_t and R_0, in contrast to equation (13). For clarity, the $Z_{in} = \omega M$ line is also drawn in figure 9. For large n, the minimum of Z_{in} near $R_t \sim 1\ \Omega$ overlaps with this line.

The performance of the TWA can be defined by the transmission coefficient T, reflection coefficient R, and radiation coefficient (or absorption coefficient) A as

$$T = \frac{P_t}{P_f} = \left| \frac{V_t}{V_f} \right|^2, \qquad (15)$$

$$R = \frac{P_r}{P_f} = \left| \frac{V_r}{V_f} \right|^2, \qquad (16)$$

$$A = 1 - (T + R), \qquad (17)$$

where P_s and V_s are the power and voltage for the forward, reflected, and transmitted waves, which are represented by the subscripts $s = f$, r, and t, respectively. The transmitted power is the power from the output port to the dummy load. In the lumped element model, T is derived from I_1 and I_n, and by using equations (9)–(11) as

$$P_t = \frac{1}{2} |I_n|^2 R_0 \qquad (18)$$

$$P_f = \frac{1}{2} \text{Re} \left[I_1^* V_{in} \right]. \qquad (19)$$

In this limited model, all of the forward power is consumed by R_t and R_0. Consequently, no reflection occurs. Figure 10 displays T in the lumped element model with $n = 7$ versus the frequency f for various R_L. The conductor resistance $R_c = 0.07\ \Omega$ is estimated by finding R_t which agrees with the

measured T in vacuum, assuming that the radiative loading can be ignored. The figure shows a typical bandpass filter characteristic with a center frequency of $f_0 = 0.5$ GHz and a bandwidth of ~ 20 MHz. Note that a combline antenna is essentially a lossy combline bandpass filter [27].

If the forward characteristic impedance is considered, the reflection R can be calculated by assuming that the characteristic impedance Z_0 is matched to Z_{in} at f_0 so that $R = |\rho|^2$, $\rho = (Z_{in} - Z_0)/(Z_{in} + Z_0)$. In this case, we can then expect a large reflection at the small R_L of figure 9, as shown in figure 11. A periodic ripple is a characteristic of a combline bandpass filter that originates from multiple resonant elements that are connected through a mutual reactance.

In this model, the effect of the radiated wave polarization is neglected. The dominant field component of the traditional combline antenna is the axial electric field, which excites the slow wave in a magnetized plasma. Therefore, a polarization modifier such as a Faraday shield, is required for fast wave coupling. In general, a Faraday shield screens out electric field components in the direction of the bar. In other words, the electric field polarization becomes perpendicular to the Faraday shield bar.

4. Experimental setup

The fabricated model of the mock-up TWA for the KSTAR vacuum vessel is shown in figure 12. The mock-up TWA was constructed from stainless steel with low power input and output ports for a low power coupling test. The dimensions of the TWA were 60 cm, 20 cm, and 5 cm in the toroidal, poloidal, and radial directions, respectively. The detailed engineering work required to provide high voltage and current standoff capability for high power was thus neglected. Thin wires were used to connect the feeding points of the first and last straps to the SMA connectors at the nearest position in the rear antenna plates. The feeding points, which required an impedance equal to the characteristic impedance of 50 Ω were determined by way of an electromagnetic simulation. As mentioned in section 3, no other matching elements are necessary. The slanted angle of the Faraday shield bar was 10°, which coincided with the magnetic pitch angle of the targeted plasma in the coupling test. The transparency and diameter of the cylindrical bar were 50% and 10 mm, respectively.

The curvature of the front surface of the TWA was consistent with a plasma equilibrium in the toroidal direction; however, the poloidal curvature of the plasma was neglected because the poloidal length of the TWA was relatively short. In the radial direction, the maximum deviation caused by neglecting the poloidal curvature was 2.2 mm in a circular plasma, which may be negligible for typical edge plasma characteristics.

The quality of the polarization achieved by the Faraday shield was evaluated through an electromagnetic simulation. Additionally, a power spectrum was deduced from the calculated electric field along a line parallel to the Faraday shield. Figure 13 shows the relative power spectrum on a line 1 cm above the Faraday shield surface for various gap distances
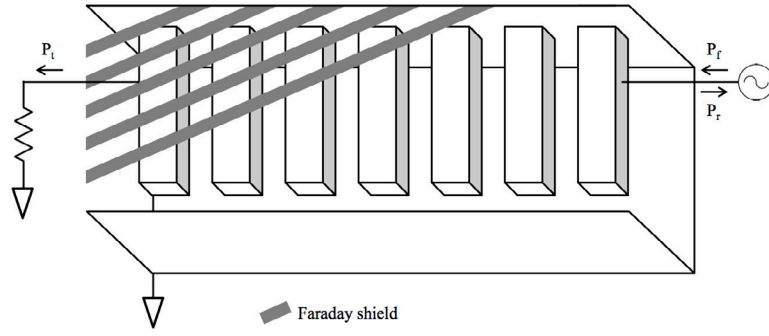
Figure 7. Illustration of a TWA with seven radiating elements. Part of the Faraday shield is indicated by the grey bars. The positions of the input and output ports have been selected to ensure a matched impedance.
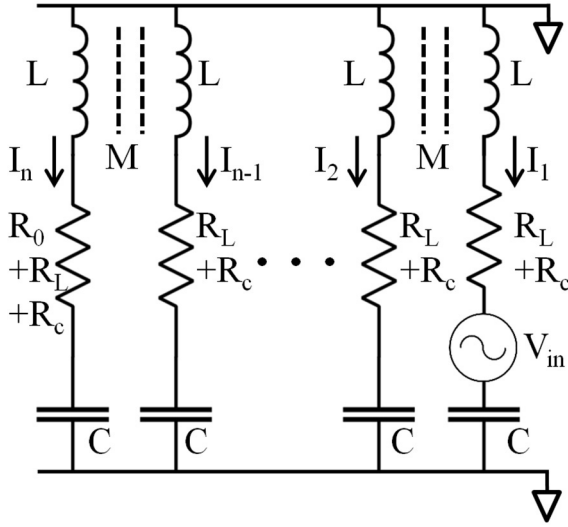
Figure 8. Simplified lumped element equivalent circuit of the TWA.
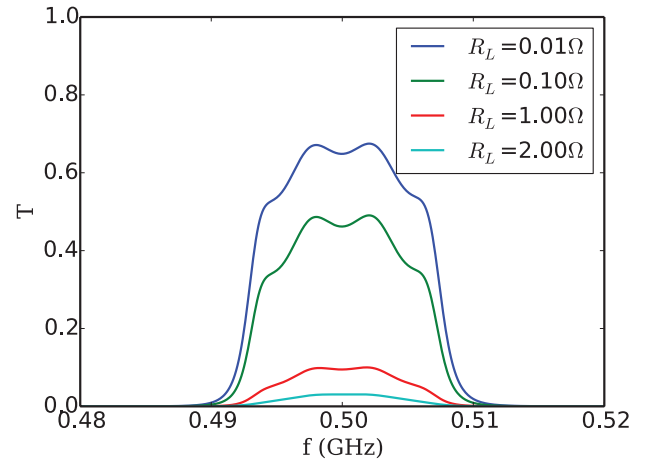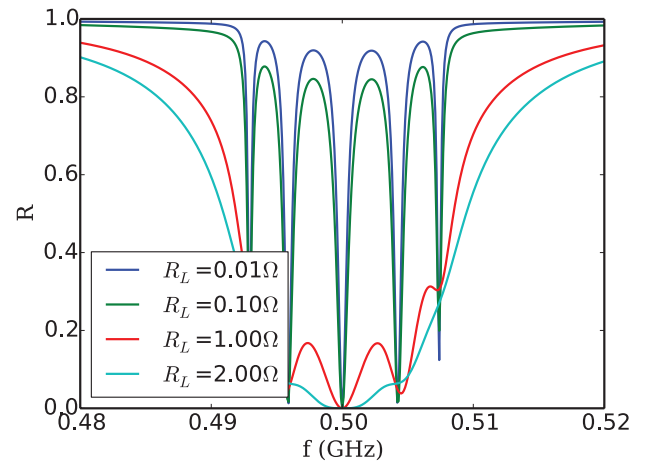

Figure 10. Power transmission of the TWA for various R_L when there is no reflection from the input.
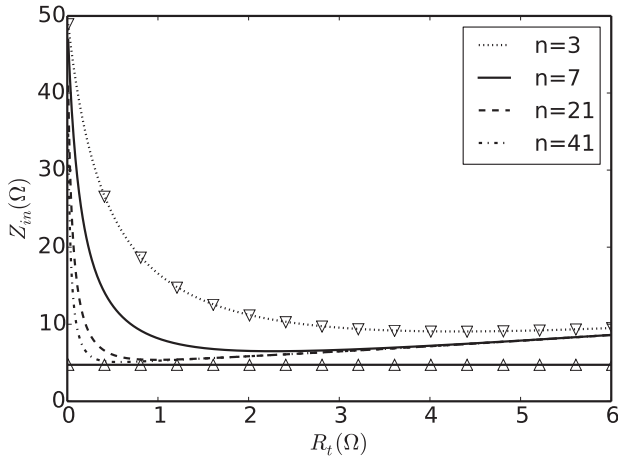
Figure 9. The input impedance Z_{in} versus the total loading resistance $R_t = R_L + R_c$ for various numbers of straps n. The line with the upright triangles represents the ωM and the line with the inverted triangles is derived from the analytic expression for $n = 3$.


Figure 11. Power reflection of the TWA for various R_L.

between the Faraday shield and the absorber. In the figure, it is evident that the peak $n_\parallel$ moves to a slightly lower value when the gap is widened. However, a large variation occurs when the gap is relatively narrow. In other words, the loading

is too high for proper operation when the loading resistance R_L cannot be ignored in comparison to the mutual reactance ωM between the neighboring straps. The detailed procedure and results of the electromagnetic simulation performed for the design of the mock-up TWA, including the Faraday shield and spectrum, will be published elsewhere.
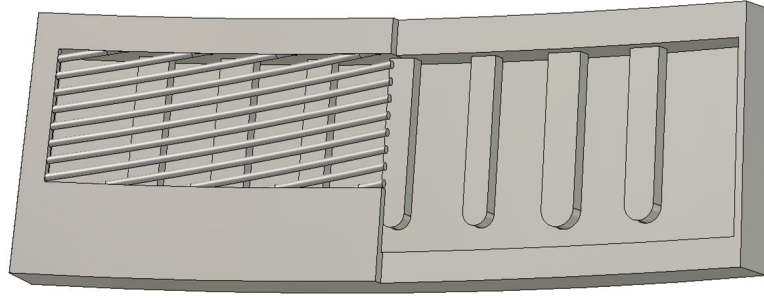
Figure 12. Model of the TWA antenna fabricated for installation in the KSTAR vacuum vessel. All parts are fabricated from stainless steel. The input and output ports are simplified for a low level coupling test. The front curvature in the toroidal direction is fitted to the off-mid-plane plasma curvature.
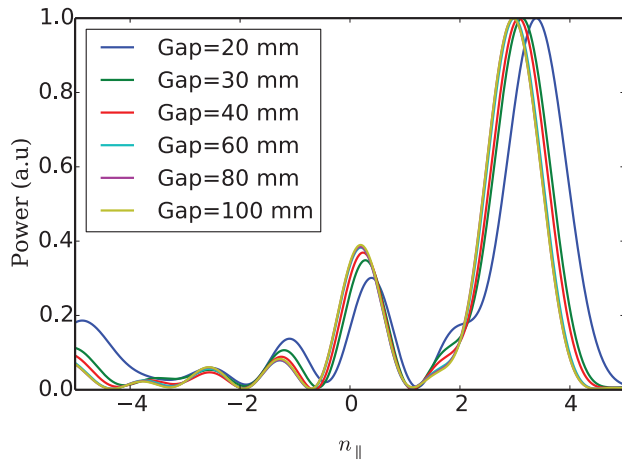

Figure 13. Calculated power spectrum of the TWA for various gaps between the front surface of the Faraday shield and the absorber. The three lines for a gap = 60–100 mm are overlapped.

The TWA was installed on the upper side of an LHCD antenna system in the KSTAR P-port, as shown in figure 14. The antenna was located at an off-mid-plane offset of 30 cm above the mid-plane. Both sides of the TWA in the toroidal direction were protected by graphite poloidal limiters, which were originally built specifically for the LHCD antenna. The radial position of the front surface of the Faraday shield was 0.5 cm behind the front surfaces of the poloidal limiters.

Dedicated local gas puffing nozzles that were constructed for the LHCD were also used to test the loading enhancement by gas injection. These formed a poloidal nozzle array with five elements located on the left side of the LHCD launcher, when viewed from the plasma side. Thus, the magnetic field did not connect the nozzles to the TWA antenna. The LHCD launcher was equipped with four electrostatic Langmuir probes at each rectangular corner that were aligned radially with the poloidal limiters. The limiter density n_{eL}, i.e. the electron density at the limiter, was estimated from the ion saturation current of the probes, assuming an electron temperature of 10 eV.

The coupling measurement was performed using a two-port Agilent E5071C network analyzer, which was connected to the TWA input and output ports. Conveniently, this network analyzer was able to simultaneously measure the forward and reflected scattering parameters, $S_{21} = V_t/V_f$ and $S_{11} = V_r/V_f$,
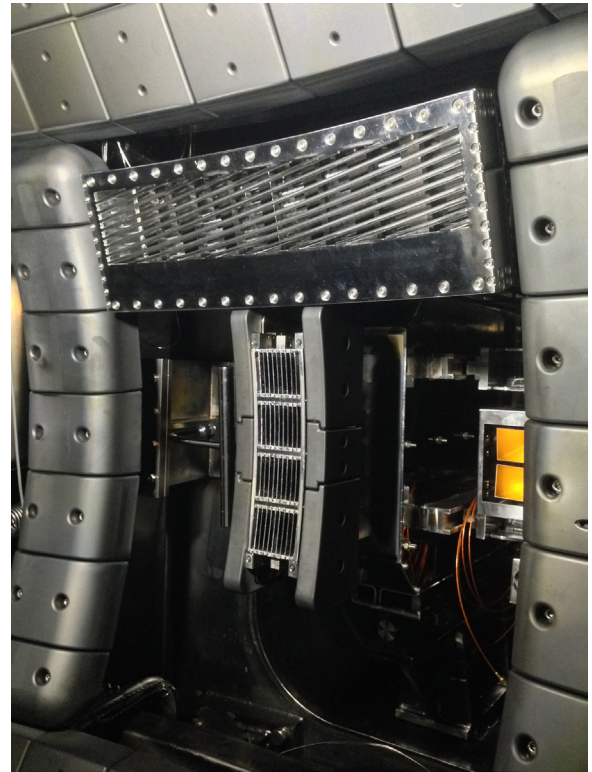
Figure 14. Installed TWA mock-up. The LHCD grill launcher at the mid-plane can be seen at the center of the photograph. Both sides of the TWA are protected by graphite poloidal limiters. The horn antennas used for millimeter-wave reflectometry are also shown. The vertical pipe attached to the left side of the LHCD grill launcher is a local gas puffing nozzle array used for the helicon coupling experiment.

for port 1 (input) and 2 (output). Note that the measurement includes lossy cables between the antenna ports and network analyzer. Figure 15 shows the scattering parameters of the TWA with and without plasma. In the plasma case, the reflection did not change meaningfully upon vacuum loading, although the transmission was significantly reduced and exhibited qualitatively large loading. The offset caused by the lossy cables, which was approximately -10 dB in every signal, was compensated for in a subsequent analysis. The compensated scattering parameter still had -1.6 dB loss, which corresponded to the finite conductor resistance $R_c = 0.07 \ \Omega$ and ignorable vacuum radiation at the operating frequency. This
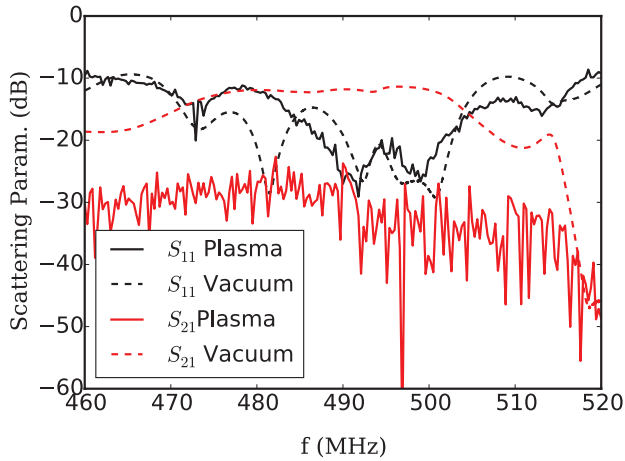
Figure 15. Scattering parameters of the two-port TWA in both vacuum and plasma measured with a network analyzer. The measurement includes lossy ($\sim$−10 dB) cables between the antenna ports and network analyzer.

conductor loss is not compensated for in a subsequent analysis, which resulted in a minimum of $A = 0.31$. The increase in the instrumentation error due to the additional lossy cable was determined to be ignorable. The measured standard deviation of noisy $|S_{21}|^2$ with −30 dB loss in this setup was 1.8×10^{-6}. However, the plasma fluctuations make it hard to accurately determine the change of R_L. The change of $A = 0.6$ to 0.63, which is believed to be detectable without statistical analysis, may be caused by the 13% increase in R_L.

5. Measurement and analysis

5.1. Radial outer-gap control

The controllability of wave coupling in the L- and H-modes of typical KSTAR plasmas was evaluated using the measured absorption coefficient A. Figure 16 shows a large increase in A during the mid-plane radial outer-gap control during the L-mode discharge #14190 from 2.5 to 7 s. The shortest distance between the front surface of the antenna and the LCFS changed from 10 to 6 cm during the change of the mid-plane outer-gap from 8 to 4 cm. A Faraday shield was aligned with the static magnetic field with a toroidal field of 1.5 T and a plasma current of 620 kA. The edge plasma density, which was estimated by the Langmuir probe at the LHCD antenna surface, increased linearly during the plasma boundary shift with a well-controlled average plasma density during flattop. The largest edge plasma density was below the fast wave cutoff density, although the absolute edge plasma density, which was calculated from the ion saturation current, is uncertain because the electron temperature was assumed to be 10 eV. Figure 17 shows similar results for an H-mode discharge #14364. In this case, the gap distance between the front surface of the antenna and the separatrix varied from 10 to 6 cm during the time period from 4 to 8 s. It must be noted that the H-mode confinement factor H_{89} remained constant during the movement of the plasma.
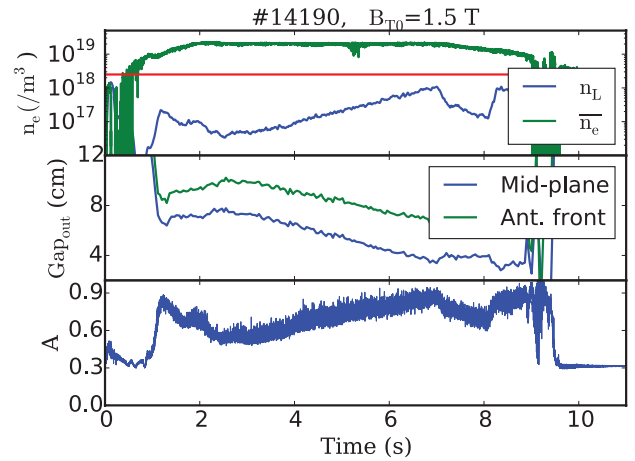
Figure 16. Evolution of the L-mode discharge #14190. The outer-gap Gap_{out} on the mid-plane is controlled from 8 to 4 cm during the time period from 2.5 to 7 s. Accordingly, Gap_{out} on the antenna front varies from 10 to 6 cm. The edge plasma density n_L is lower than the fast wave cutoff density, as illustrated by the red horizontal line in the n_e panel.
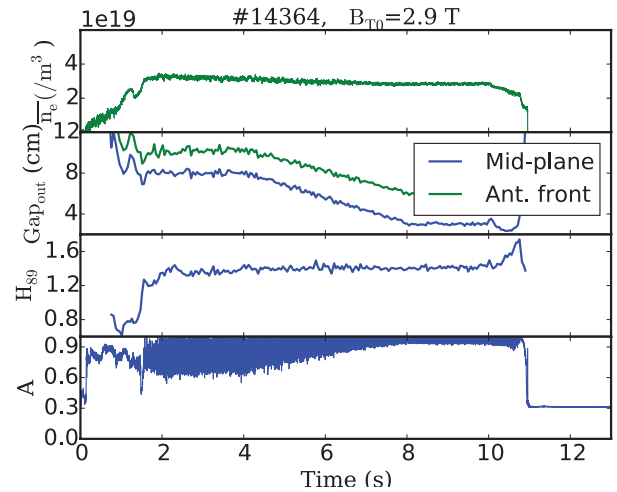
Figure 17. Evolution of H-mode discharge #14364. The outer-gap Gap_{out} on the mid-plane is controlled from 8 to 3 cm during the time period from 4 to 8 s. Accordingly, Gap_{out} on the antenna front varies from 10 to 6 cm. The H-mode confinement factor H_{89} does not decrease during large movements of the plasma.

The interpretation of the absorption coefficient A in H-mode requires caution. The waveform of A behaves similarly to the D_α signal because a high electron density in front of the antenna during ELM causes a large loading in both fast and slow waves as well as the other stray loading such as collisional heating [28, 29]. Therefore, a meaningful A may be the bottom of thick A that is close to an average A during a period of ELM. The detailed waveform of A will be shown in the later section that discusses load resiliency. The bottom of A increases considerably and almost linearly during the boundary movement without severe degradation of the plasma confinement. This means that the power coupling of the helicon wave may be easily controlled by changing the radial outer-gap in KSTAR plasmas.

Figure 18 shows a comparison of the measurements in H-mode discharge #14364 with the analytic calculation of the absorption coefficient A and phase difference $\Delta\Phi$ between the forward and transmitted voltages. The A and $\Delta\Phi$ calculated using an electromagnetic simulation with an absorber is also shown for reference. An analytical values are derived by combining $R_{L\alpha}$ from the surface impedance analysis and A from TWA theory. The distance d is the gap between the Faraday shield and the slab plasma with a density of $4 \times 10^{18}\,\text{m}^{-3}$ in the analytical case, the absorber surface in the electromagnetic simulation, and the estimated plasma position where the density is the same as in the analytical case for the measurement in H-mode plasma. The density position was estimated by assuming a bi-linear density profile from the pedestal top to the limiter. The density at the pedestal top and the limiter are measured using Thomson scattering and a Langmuir probe, respectively, and the density at the separatrix and the density width are calculated from the scaling in reference [30]. While considering the large errors between the assumed and estimated density profiles, the bottom of the measured A in H-mode discharge is in reasonable agreement with the surface impedance analysis. At small d, A decreases slowly and $\Delta\Phi$ increases rapidly as d increases, and at large d, the trends are reversed. Also, at small d, there is a large contribution from the slow wave, which means that strong coupling with a short gap should be avoided in order to prevent parasitic loading and phase change, which will be discussed further in a later section. The increasing discrepancy at large d suggests that more elaborate models for loading resistance and antenna systems may be required.
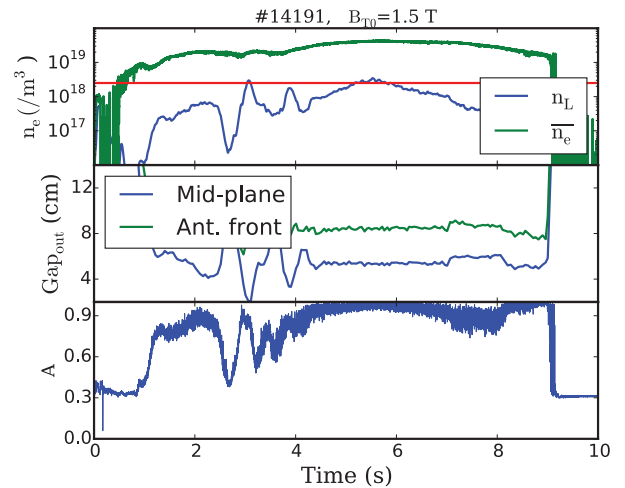
5.2. Local gas puffing

Local gas puffing is known to be a strong actuator for controlling the power coupling in ICRF [31] and LHCD [32, 33] heating and current drives. The strategy followed in local gas injection entails puffing the minimal amount of gas from a gas nozzle that is magnetically connected to the antenna surface in order to increase the plasma density locally in front of the antenna. A minimal amount of gas is required to minimize plasma confinement degradation and a negative effect on the wave propagation. The increase in the density between the antenna and the bulk plasma increases both the fast wave couplings in the ICRF and the helicon wave, and slow wave couplings in the LHCD by reducing the thickness of the evanescent layer. However, the increase in the local density in high harmonic fast wave heating has been reported to cause strong SOL losses [28, 29]. A high density in the LHCD regime seems to cause nonlinear phenomena [34, 35], which must be avoided to achieve an appropriate power coupling to a bulk plasma.

The evolution of the L-mode discharge #14191 with local gas puffing over a duration 3.5–5.5 s is shown in figure 19. The gas flow rate is $5 \times 10^{21}\,\text{el s}^{-1}$. During gas injection, both the average density $\bar{n}_e$ and the limiter density n_{eL} continuously increase while Gap_{out} at the mid-plane and the front surface of the antenna remains relatively constant, as long as the large
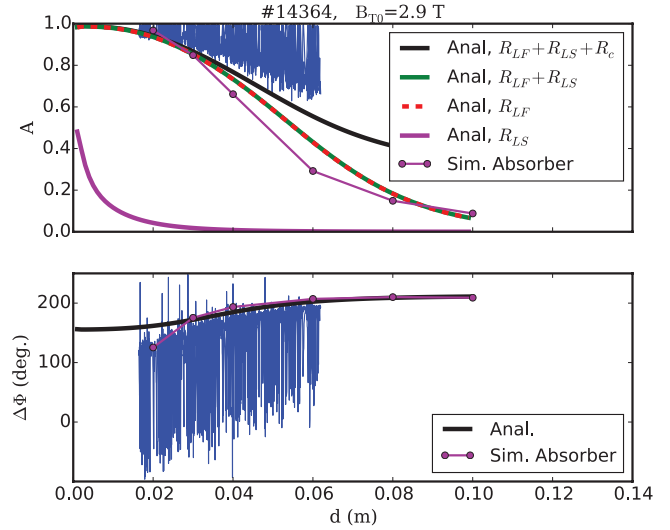

Figure 18. Absorption A and phase difference $\Delta\Phi$ as functions of the gap d for different cases: surface impedance analysis, electromagnetic simulation with an absorber, and H-mode discharge #14364. The analytic A for the fast wave and that for both waves are almost overlapped. The bottom of the thick A and the top of the thick $\Delta\Phi$ correspond to the baseline of the ELMy plasma.

Figure 19. Evolution of the L-mode discharge #14191 at $B_{T0} = 1.5\,\text{T}$. Local gas puffing is examined from 3.5 to 5.5 s through nozzles located on the side of the LHCD antenna. The fast wave cutoff density is indicated by the red horizontal line in the n_e panel.

fluctuations before 4.3 s are disregarded. It must be noted that no abrupt change of A is observed when the limiter density n_{eL} surpasses the fast wave cutoff density at 5.5 s. The absorption coefficient A also increases up to 0.9. The evolution of the H-mode discharge #14365 also shows a strong dependency of the absorption coefficient A on gas puffing, as displayed in figure 20. Gas puffing with a flow rate of 2×10^{21} el s^{-1} was applied from 4 to 8 s. The local gas flow rate during this discharge was much smaller than that in the L-mode #14191 case. During H-mode gas puffing, the average density $\bar{n}_e$ increased very slowly, while the absorption coefficient increased significantly up to 0.8. It was observed that the total decrease of H_{89} was approximately 13%.
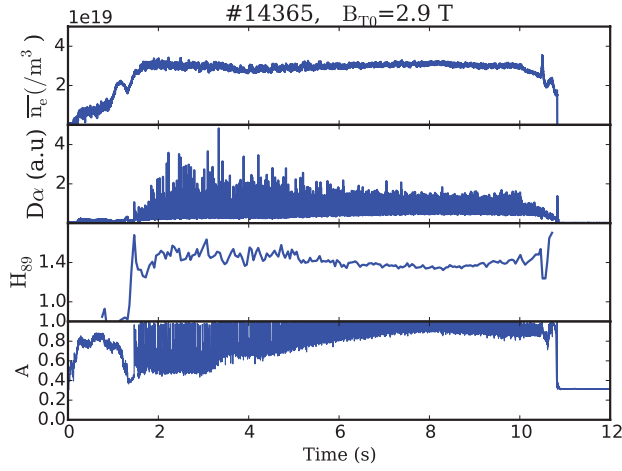
Figure 20. Evolution of the H-mode discharge #14365 at $B_{T0} = 2.9$ T. Local gas puffing was applied from 4 to 8 s.

Figure 21. Evolution of the plasma parameters and coefficient A and R in ELMy H-mode #14192 at $B_{T0} = 1.5$ T.

5.3. Load resiliency

Large reflections always cause problems in RF heating systems because they can cause power reductions from RF amplifiers or generators, and damage to transmission lines and power sources. Static matching does not solve these problems because the antenna input impedance changes rapidly during changes in the edge plasma status, such as L/H mode transitions and ELMs. In these applications, a TWA is a suitable antenna system because input impedance is insensitive to the loading resistance, as shown in figure 9. Therefore, if the variation of the loading resistance remains within a defined range, there is no problematic reflection. This is a great advantage of the TWA. In addition, the fact that no matching system is required is also an advantage because mechanical matching systems are problematic components in MW-level RF systems.

Figure 21 shows the evolution of discharge #14192. The H-mode ELM signature in D_α is observed after 1 s. The limiter density n_{eL} also implies that strong density bursts occur, in accordance with the ELM. The absorption coefficient A and phase difference $\Delta\Phi$ also show similar fluctuations. Figure 22 shows an expansion of the waveform of #14192 during the L/H transition, including the details of its evolution during ELM bursts. During small D_α bursts, n_{eL} and A show similar trends. However, the baseline of A is not much smaller than that observed in the L-mode before <1.36 s. Additionally, a small reflection coefficient R appears during the short period of n_{eL} as it approaches its top. However, the average value of R may be negligible. The fluctuation of the phase difference between the input and output ports, $\Delta\Phi$ can create confusion, and it is uncertain whether the change of $\Delta\Phi$ is caused by the change of phase speed in guided traveling waves in the TWA or by measurement error due to the very small coupled signal from the output port. Note that $A = 1$ means that no power appears at the output port. The latter explanation is highly possible because the deviation of $\Delta\Phi$ seems to imply a threshold for A.

From these results, it can be concluded that the TWA is resilient to the L/H mode transition and ELMs. Small reflections during short periods can be circulated by a circulator or a hybrid decoupler.
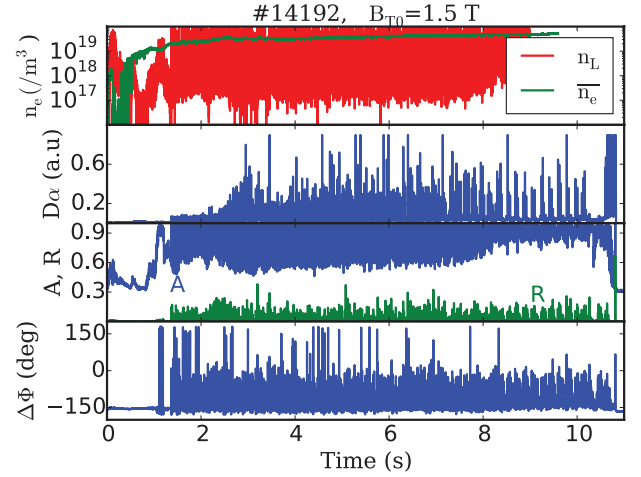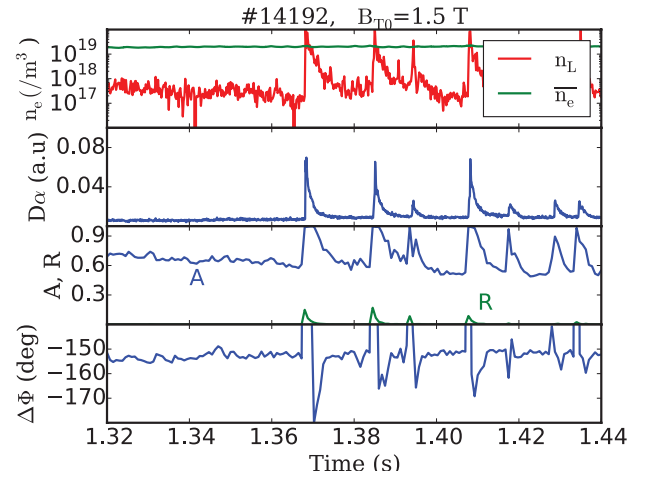

Figure 22. Detailed evolution of #14192 showing L-/H-mode transition and ELMs.

5.4. Refractive index

The parallel refractive index $n_\parallel$ is one of the most important parameters for controlling wave propagation or damping. Therefore, it must be effectively regulated. The phase difference $\Delta\Phi$ between the forward and transmitted voltage is linearly related to $n_\parallel$ as $n_\parallel = (\Delta\Phi/l)(c/\omega)$, where l is the active axial length of the antenna. Figure 23 shows that both the simulation and H-mode plasma discharge results determined that $\Delta\Phi$ is stable when the absorption coefficient is below a certain value, namely $A < 0.7$. The decrease of $\Delta\Phi$ above this value is caused by the distortion of the relationship between the loading resistance R_L at each strap and the mutual inductance M between adjacent straps.

5.5. Faraday shield alignment

As discussed in section 2, there has been considerable concern about stray coupling through slow wave. To identify slow wave coupling, the magnetic pitch angle was scanned during a
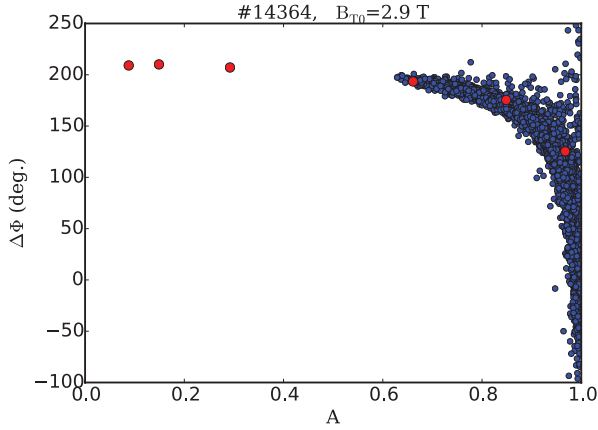
Figure 23. Antenna phase difference versus absorption coefficient for H-mode discharge #14364 (blue dots) and the antenna simulation with an absorber in front of the antenna (red dots).
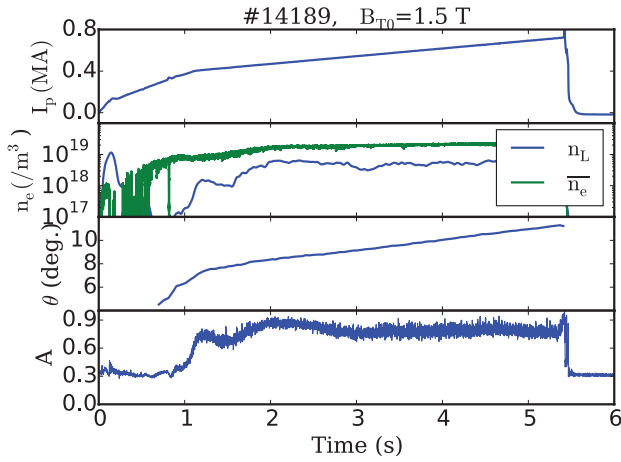
Figure 24. Magnetic pitch scan performed by increasing the plasma current I_p in the NBI heated L-mode discharge #14189 at $B_0 = 1.5$ T. The safety factor q_{95} decreases accordingly from 1 to 5.5 s. The last closed flux surface at $R = 2.26$ m and the average plasma density remain constants from 2 to 5.5 s. The variation of the magnetic pitch angle from 8° to 12° surpasses the 10° tilt angle of the Faraday shield.

discharge for both the L- and H-mode, as shown in figures 24 and 25. To obtain the widest possible range of pitch angles in front of the antenna, the plasma current I_p was ramped from 400 to 710 kA and to 800 kA at $B_0 = 1.5$ T for the L- and H-mode discharges, respectively. At the highest I_p, the safety factor q_{95} decreased below 3.

During the L-mode discharge #14189, the radial position of the last closed flux surface R_{out} and average electron density $\bar{n}_e$ remained constant from 2 to 5.5 s. Notably, the coefficient A is very high, approximately 0.85, and no apparent relationship exists between the pitch angle and A. In the H-mode discharge #14192, the bottom of the coefficient A also shows no correlation with the pitch angle, while a slow increase of $\bar{n}_e$ and a small fluctuation of the separatrix position R_{out} are observed. The large fluctuation of A is caused by the density peaking in front of the antenna during ELM bursts. Therefore,
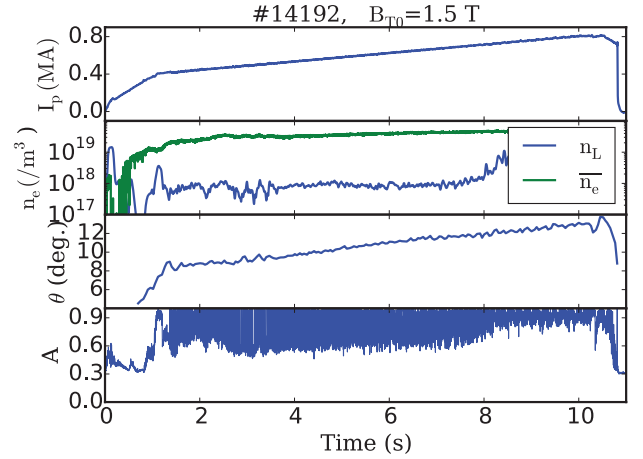
Figure 25. Magnetic pitch scan performed by increasing the plasma current I_p in the NBI heated H-mode discharge #14192 at $B_0 = 1.5$ T. The safety factor q_{95} decreases accordingly up to 10 s. The mid-plane separatrix at $R = 2.26$ m is relatively stable, while the average density $\bar{n}_e$ increases continuously. The variation of the magnetic pitch angle from 8.5° to 13° surpasses the 10° tilt angle of the Faraday shield.

a much smaller baseline A than that of the L-mode can be estimated. Details on the behavior of A during ELM bursts are provided in section 5.3. In the limited range of angle differences between the Faraday shield and the magnetic field examined in these measurements, there was no indication of slow wave coupling. These results agree with an evaluation conducted using an R_L analysis based on the surface impedance. It must be noted that it is not practical to expect much larger angle differences in normal plasma operations intended for helicon wave coupling.

6. Summary and conclusion

The helicon wave coupling to the KSTAR plasma was analyzed through a surface impedance analysis and low power experiments. The surface impedance analysis showed that the slow wave, which may be an unfavorable mode for a helicon wave current drive, can be coupled to the plasma when parallel electric field components exist at the antenna surface. The slow wave coupling increases when mode coupling is engaged. The mode coupling term expressed in this article is a phenomenon in which a parallel electric field is generated or enhanced as a result of the off-diagonal elements in a plasma impedance matrix, even if there are small or non-existent relevant antenna current components.

However, in the analytic calculation, the slow wave contribution to the loading resistance R_{LS} was lower than that for the fast wave R_{LF} by more than an order of magnitude when the electron density was moderate at the plasma boundary, $n_e > 1 \times 10^{18}$ m^{-3}, and the pitch angle misalignment was less than 10°. If $n_e = 3 \times 10^{18}$ m^{-3}, the R_{LS} portion was still below 10% if the misalignment was lower than 45°. In addition, the measurement also did not show any evidence of significant slow wave coupling when the pitch angle was scanned.

The low level RF characteristics of the fabricated low power TWA were in good agreement with the designed characteristics in terms of the two-port scattering matrix with the center frequency and bandwidth. The TWA, which was installed at an off-mid-plane, also showed good coupling capability in L- and H-mode plasmas. The traditional means to control RF couplings were effective. The control of the radial outer-gap by moving the plasma outer boundary from 8 to 4 cm at the mid-plane in the L- and H-mode discharges doubled the coupling defined by the absorption coefficient A almost linearly. Hardly any plasma confinement degradation was observed during plasma movement. Local gas puffing was also quite effective in enhancing the coupling, although the gas nozzle was not magnetically connected to the antenna surface. The small degradation of the confinement, 13% of H_{89}, was observed during gas puffing.

In principle, the TWA is load resilient to a certain extent. A coupling measurement in an ELMy H-mode discharge showed that the TWA is resilient to L-/H-mode transition and ELMs. The small reflections that appeared during short periods of large ELM bursts can be circulated by a circulator or hybrid decoupler.

It was determined that too much coupling is a possible problem for accurately maintaining the parallel refractive index $n_\parallel$. This is because a large loading distorts the assumed relationship between a small loading resistance and the mutual reactance, $R_L \ll \omega M$, which results in distortion of the phase relationship between the radiating straps. A much larger number of straps with small loading can solve this issue.

The surface impedance model which was analyzed to discuss the measured results is limited to the cold plasma wave without collision. Therefore, it is highly possible that there are additional loss channels, particularly in between the antenna and plasma due to the high neutral and plasma density. These additional losses may eliminate small gap between the model and the measurement, especially at the low loading as shown in figure 18. In addition, for a realistic plasma boundary having broad transition, connecting method like using Airy function is required as discussed in reference [14]. The model used in this analysis may be applicable to the step change or steep gradient of the refractive index at plasma boundary.

Acknowledgments

Appendix

If the tangential electric and magnetic fields are defined as

$$\mathbf{E}_t = \begin{pmatrix} E_y \hat{y} \\ E_z \hat{z} \end{pmatrix}, \tag{A.1}$$

$$\mathbf{B}_t = \begin{pmatrix} B_z \hat{y} \\ -B_y \hat{z} \end{pmatrix}, \tag{A.2}$$

the surface impedance and admittance at $x = 0$, $\mathbf{Z}^p$, $(\mathbf{Z}^p)^{-1} = \mathbf{Y}^p$ are expressed by the proportional matrix of the tangential fields.

$$\mathbf{E}_t^0 = \mathbf{Z}^p \cdot \mathbf{B}_t^0, \tag{A.3}$$

$$\mathbf{B}_t^0 = \mathbf{Y}^p \cdot \mathbf{E}_t^0. \tag{A.4}$$

The analytical expression of the surface impedance $\mathbf{Z}^p$ in CGS units is

$$\mathbf{Z}^p = \frac{1}{\Delta} \begin{pmatrix} b_y^F e_y^S - b_y^S e_y^F & b_z^F e_y^S - b_z^S e_y^F \\ b_y^F e_z^S - b_y^S e_z^F & b_z^F e_z^S - b_z^S e_z^F \end{pmatrix}, \tag{A.5}$$

$$\Delta = b_y^F b_z^S - b_y^S b_z^F. \tag{A.6}$$

The polarization vectors with n_y are obtained from the rotational transform $\mathbf{R}^\alpha$ of vectors with $n_y = 0$, where α denotes the fast (F) or slow (S) mode.

$$\mathbf{e}^\alpha = \mathbf{R}^\alpha \mathbf{e}^\alpha(0), \tag{A.7}$$

$$\mathbf{b}^\alpha = \mathbf{R}^\alpha \mathbf{b}^\alpha(0), \tag{A.8}$$

$$\mathbf{R}^\alpha = \begin{pmatrix} n_{x\alpha}/n_{\perp\alpha} & n_{y\alpha}/n_{\perp\alpha} & 0 \\ -n_{y\alpha}/n_{\perp\alpha} & n_{x\alpha}/n_{\perp\alpha} & 0 \\ 0 & 0 & 1 \end{pmatrix}. \tag{A.9}$$

The Maxwell equations with $n_y = 0$ yield

$$e_y^F(0) = k_F(n_{\perp F}^2 - n_{\perp S}^2), \tag{A.10}$$

$$e_z^F(0) = i k_F n_z n_{\perp F} \frac{D}{S}, \tag{A.11}$$

$$e_y^S(0) = i k_S n_z \frac{D}{n_z^2 - S} n_{\perp S}, \tag{A.12}$$

$$e_z^S(0) = k_S(n_{\perp S}^2 - n_{\perp F}^2), \tag{A.13}$$

where k_F and k_S are normalization factors. The tangential magnetic field components are related to the tangential electric fields as

$$b_z^\alpha(0) = n_{\perp\alpha} e_y^\alpha(0), \tag{A.14}$$

$$b_y^\alpha(0) = \frac{n_{\perp\alpha} S e_z^\alpha(0) - i n_z D e_y^\alpha(0)}{n_z^2 - S}, \tag{A.15}$$

and the normal components are

$$e_x^\alpha(0) = \frac{1}{S} \left[i D e_y^\alpha(0) + n_z b_y^\alpha(0) \right], \tag{A.16}$$

$$b_x^\alpha(0) = -n_z e_y^\alpha(0). \tag{A.17}$$

The off-diagonal terms in $\mathbf{Z}^p$ in equation (A.5) indicate that the fast or slow waves are coupled to their respective counter-parts. If e_z^F, e_y^S, b_z^S, and b_y^F, which can be small compared to their counter-part vectors with the same directions, are neglected, $\mathbf{Z}^p$ can be completely decoupled from each of the other modes. The decoupled surface impedance, i.e. $Z_F = e_y^F/b_z^F$, $Z_S = -e_z^S/b_y^S$, is convenient for studying the effect of the coupled modes.

Considering the WKB approximation in vacuum at $x < 0$, the tangential electric field can be written as

$$\mathbf{E}_t = [\exp(\mathrm{i}k_0\nu_\perp x)\mathbf{1} + \exp(-\mathrm{i}k_0\nu_\perp x)\boldsymbol{\rho}] \cdot \boldsymbol{\alpha}, \tag{A.18}$$

where the reflection coefficient $\boldsymbol{\rho}$ is

$$\boldsymbol{\rho} = (\mathbf{Y}^v + \mathbf{Y}^p)^{-1} \cdot (\mathbf{Y}^v - \mathbf{Y}^p), \tag{A.19}$$

and the vacuum admittance $\mathbf{Y}^v = (\mathbf{Z}^v)^{-1}$ can be easily obtained by using the electron density $n_e = 0$ in equation (A.5) or

$$\mathbf{Z}^v = \frac{1}{\nu_x}\begin{pmatrix} 1 - n_y^2 & -n_y n_\parallel \\ -n_y n_z & 1 - n_z^2 \end{pmatrix}. \tag{A.20}$$

If the electric field vectors at the antenna $x = -x_a$ are written as [14]

$$\mathbf{E}_t^a = \frac{\pi \mathrm{i}}{c}\frac{J_a}{n_\perp}\{1 - \exp\left[-2k_0 n_\perp(x_w - x_a)\right]\}\begin{pmatrix} \cos(\phi)\hat{y} \\ \sin(\phi)\hat{z} \end{pmatrix}, \tag{A.21}$$

where ϕ is the angle difference between the normal antenna current density J_a and the z direction, then $\boldsymbol{\alpha}$ can be easily obtained using the excitation equation (A.21) and assuming

$$\mathbf{E}_t(x = -w_a) = \mathbf{E}_t^a. \tag{A.22}$$

Because the tangential electric field is continuous across the plasma boundary at $x = 0$, $\mathbf{E}_t$ in equation (A.1) and $\mathbf{Z}^p$ in equation (A.5) can be used to obtain the power coupled to the plasma using the Poynting flux at $x = 0$ expressed in CGS units as

$$P_x = \frac{c}{8\pi}\mathrm{Re}\left[(\mathbf{E}_t^0)^* \cdot \mathbf{B}_t^0\right]. \tag{A.23}$$

As the electric and magnetic fields are defined unconventionally by equations (A.1) and (A.2), the terms in equation (A.23) may be separated into the X- and O-mode contributions as

$$P_{xF} = \frac{c}{8\pi}\mathrm{Re}\left[E_y^* B_z\right], \tag{A.24}$$

$$P_{xS} = \frac{c}{8\pi}\mathrm{Re}\left[-E_z^* B_y\right]. \tag{A.25}$$

From these power contributions, the loading resistances for each mode can be derived by using antenna current.

References

[1] Jardin S.C., Kessel C.E., Bathke C.G., Ehst D.A., Mau T.K., Najmabadi F., Petrie T.W. and ARIES Team 1997 Physics basis for a reversed shear tokamak power plant *Fusion Eng. Des.* **38** 27
[2] Oikawa T. *et al* 2001 *Nucl. Fusion* **41** 1575
[3] Franzen P. and Fantz U. 2014 *Fusion Eng. Des.* **89** 2594
[4] Garcia J., Artaud G.G.J., Basiuk V., Decker J., Imbeaux F., Peysson Y. and Schneider M. 2008 *Nucl. Fusion* **48** 075007
[5] Lerche E., Van Eester D., Messiaen A., Franke T. and EFDA-PPPT contributors 2014 Fast wave current drive in DEMO *AIP Conf. Proc.* **1580** 338
[6] Franke T. *et al* 2014 RF H&CD systems for DEMO—challenges and opportunities *AIP Conf. Proc.* **1580** 207
[7] Gormezano C. 1986 *Plasma Phys. Control. Fusion* **28** 1365
[8] Hillairet J. *et al* 2013 *Nucl. Fusion* **53** 073004
[9] Hooke W. 1984 *Plasma Phys. Control. Fusion* **26** 133
[10] Koch R., Lerche E., Van Eester D., Nightingale M., Phillips C. K. and Wilson J. R. 2011 High frequency fast wave current drive for DEMO *AIP Conf. Proc.* **1406** 349
[11] Vdovin V.L. 2013 *Plasma Phys. Rep.* **39** 95–115
[12] Prater R., Moeller C.P., Pinsker R.I., Porkolab M., Meneghini O. and Vdovin V.L. 2014 *Nucl. Fusion* **54** 083024
[13] Wang S.J., Kim J., Jeong J.H., Kim H.J., Joung M., Bae Y.S. and Kwak J.G. 2015 Recent experimental results of KSTAR RF heating and current drive *AIP Conf. Proc.* **1689** 030014
[14] Bilato R., Brambilla M., Hartmann D.A. and Parisot A. 2005 *Nucl. Fusion* **45** L5–7
[15] Moeller C.P., Gould R.W., Phelps D.A. and Pinsker R.I. 1994 Combline antennas for launching traveling fast waves *AIP Conf. Proc.* **289** 323
[16] Pinsker R.I. *et al* 1996 Development of fast wave systems tolerant of time-varying loading *Proc. 19th Symp. on Fusion Techology (Lisbon, Portugal, 16−20 September 1996)* vol 1, ed C. Varandas *et al* (Elsevier) p 629
[17] Ikezi H. and Phelps D.A. 1997 *Fusion Sci. Technol.* **31** 106–17 (www.ans.org/pubs/journals/fst/a_30782)
[18] Takeuchi N. *et al* 2002 *J. Plasma Fusion Res. Ser.* **5** 314 (www.jspf.or.jp/JPFRS/PDF/Vol5/jpfrs2002_05-314.pdf)
[19] Stix T.H. 1975 *Nucl. Fusion* **15** 737
[20] Hellsten T., Eriksson L.G. 1991 An analysis of trapped particle effects on fast wave current profiles *Proc. IAEA Technical Committee Meeting on Fast Wave Current Drive in Reactor Scale Tokamaks (Synergy and Complementarity with LHCD and ECRH) (Arles, France, 23−25 September 1991)* ed D. Moreau *et al* p 48
[21] Vdovin V.L. 1983 *Nucl. Fusion* **23** 1435
[22] Pury S. 1983 *Phys. Fluids* **26** 164
[23] Brambilla M. 1995 *Nucl. Fusion* **35** 1265
[24] Bak J.G. *et al* and The KSTAR Project Team 2013 *Contrib. Plasma Phys.* **53** 69
[25] Ogawa T. *et al* 2001 *Nucl. Fusion* **41** 1767
[26] Pinsker R.I. 1998 *Plasma Phys. control. Fusion* **40** A215
[27] Jones E.M.T. 1956 *IEEE Trans. Microw. Theory Tech.* **4** 75–81
[28] Perkins R.J. *et al* 2012 *Phys. Rev. Lett.* **109** 045001
[29] Bertelli N. *et al* 2016 *Nucl. Fusion* **56** 016019
[30] Kallenbach A., Asakura N., Kirk A., Korotkov A., Mahdavi M.A., Mossessian D. and Porter G.D. 2005 *J. Nucl. Mater.* **337–9** 381
[31] Jacquet P. *et al* 2016 *Nucl. Fusion* **56** 146001
[32] Ekedahl A. *et al* 2005 *Nucl. Fusion* **45** 351
[33] Ekedahl A. *et al* 2012 *Plasma Phys. Control. Fusion* **54** 074004
[34] Takase Y., Porkolab M., Schuss J.J., Watterson R.L., Fiore C.L., Slusher R.E. and Surko C.M. 1985 *Phys. Fluids* **28** 983
[35] Wallace G.M. *et al* 2011 *Nucl. Fusion* **51** 083032